Isolas of 2-Pulse Solutions in Homoclinic Snaking Scenarios

**Jürgen Knobloch · David J. B. Lloyd ·
Björn Sandstede · Thomas Wagenknecht**

Abstract Homoclinic snaking refers to the bifurcation structure of symmetric localised roll patterns that are often found to lie on two sinusoidal "snaking" bifurcation curves, which are connected by an infinite number of "rung" segments along which asymmetric localised rolls of various widths exist. The envelopes of all these structures have a unique maximum and we refer to them as symmetric or asymmetric 1-pulses. In this paper, the existence of stationary 1D patterns of symmetric 2-pulses that consist of two well-separated 1-pulses is established. Corroborating earlier numerical evidence, it is shown that symmetric 2-pulses exist along isolas in parameter space that are formed by parts of the snaking curves and the rungs mentioned above.

Keywords Homoclinic snaking · Isolas · Multi-pulses · Swift–Hohenberg equation

1 Introduction

The emergence of localised patterns in bistable systems has attracted much attention in recent years with particular emphasis being given to the phenomenon known as homoclinic snaking. This phenomenon refers to the appearance and disappearance of infinitely many stationary localised patterns through virtually simultaneous saddle-node bifurcations and, more specifically, to the property that all these emerging patterns are globally connected in parameter

J. Knobloch
Department of Mathematics, Technical University Ilmenau, 98684 Ilmenau, Germany

D. J. B. Lloyd
Department of Mathematics, University of Surrey, Guildford GU2 7XH, UK

B. Sandstede (✉)
Division of Applied Mathematics, Brown University, Providence, RI 02912, USA
e-mail: bjorn_sandstede@brown.edu

T. Wagenknecht
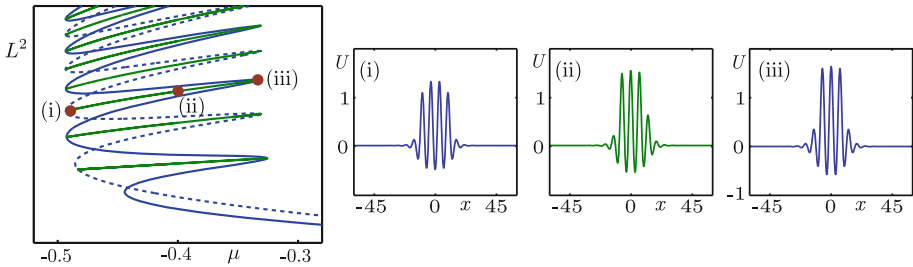Department of Applied Mathematics, University of Leeds, Leeds LS2 9JT, UK

Fig. 1 In the *left panel*, the L^2-norm of 1-homoclinic orbits of the Swift–Hohenberg equation (1.1) is plotted against the parameter μ. The three panels to the *right* show the solution profiles $U(x)$ as functions of x along one of the rungs that connect the two *snaking curves* that are plotted as *solid* and *dashed curves*

space. In particular, there is an open region in parameter space in which infinitely many localised patterns coexist. The interior part of these patterns resembles a spatially periodic structure, so that one can interpret them as periodic waves that are subjected to a localised amplitude modulation. As one follows these patterns in the bifurcation parameter, their interior domain broadens indefinitely.

In this paper, we focus on one-dimensional patterns. As an example, consider the Swift–Hohenberg equation

$$U_t = -(1 + \partial_x^2)^2 U + \mu U + \nu U^2 - U^3, \quad x \in \mathbb{R}, \ U \in \mathbb{R}$$

with $\nu = 2$. Stationary localised patterns of the Swift–Hohenberg equation with $\nu = 2$ can be computed as homoclinic orbits of the steady-state equation

$$(1 + \partial_x^2)^2 U - \mu U - 2U^2 + U^3 = 0 \tag{1.1}$$

or, equivalently, of the associated first-order system

$$u_x = f(u, \mu), \quad u = (u_1, u_2, u_3, u_4)^T = (U, U_x, U_{xx}, U_{xxx})^T \in \mathbb{R}^4$$

with

$$f(u, \mu) = (u_2, u_3, u_4, -2u_3 + (\mu - 1)u_1 + 2u_1^2 - u_1^3)^T.$$

Homoclinic snaking in (1.1) has been discussed in a number of papers, and we refer to [2,4] for a comprehensive list of references and to [11,16] for two recent reviews that also list numerous applications in the natural sciences. The characteristic bifurcation diagram for 1-homoclinic orbits to the origin is shown in Fig. 1. It consists of two intertwined snaking curves corresponding to homoclinic orbits of (1.1) that are symmetric under the reflection $x \mapsto -x$: as shown in the rightmost panels in Fig. 1, the symmetric orbits along the two different snaking curves differ by whether they are symmetric about a maximum or minimum. The two snaking curves are connected by rungs or ladders that correspond to non-symmetric homoclinic orbits. We refer to the union of the two snaking curves and the rung branches as the double-helix structure.

The geometric foundation of homoclinic snaking is well understood. The homoclinic orbits bifurcate from a heteroclinic cycle that is formed by connecting orbits between the equilibrium $U = 0$ and a periodic orbit. A geometric explanation of snaking, based on a careful inspection of the intersections of the stable and unstable manifolds of the underlying equilibrium and periodic orbits, has been given in [25]; see also [10]. For the special case of the Swift–Hohenberg equation, this picture has been put on a firm footing in [9,18] using

normal-form theory and beyond-all-orders asymptotics. On a general level, the precise link between the global geometry of the heteroclinic connections and the resulting snaking diagrams of both symmetric and non-symmetric solutions has been elucidated in [2]. From a structural viewpoint, the key ingredients necessary for snaking to occur are reversibility (that is, the invariance under reflection in x) and, to some extent, the property that the underlying equation is conservative or Hamiltonian. If the system is not conservative, then snaking may still occur but the non-symmetric solutions will, in general, correspond to travelling waves and not to stationary states.

The papers mentioned above focused on 1-homoclinic orbits, that is, on homoclinic solutions that follow the underlying heteroclinic cycle precisely once. The general bifurcation results by Devaney [12] or Härterich [13] imply that each of the 1-homoclinic orbits described above will, for each fixed parameter value, be accompanied by families of N-homoclinic solutions that follow the heteroclinic cycle precisely N times provided the underlying equilibrium is a bi-focus. The results in [12,13] also indicate that, for each N, there will be infinitely many N-homoclinic orbits that differ by the separation distances between consecutive pulses. Our goal is to analyse their existence in homoclinic snaking scenarios, where the 1-homoclinic orbits arise in global bifurcations from heteroclinic cycles. We shall focus on symmetric 2-homoclinic orbits.

Multi-pulse solutions in snaking scenarios were first studied numerically in [14,24], where it was observed that 2-pulse solutions lie on closed curves near the original snaking curves. Various different types of isolas that differed by the number of fold bifurcations they contained were found in these two papers. To gain further insight into 2-pulse solutions, we computed symmetric 2-homoclinic orbits for the Swift–Hohenberg equation (1.1) using the homoclinic branch-switching method developed in [21] and show the resulting bifurcation diagram and the associated solution profiles in Fig. 2. This diagram shows the double helix of symmetric and non-symmetric 1-pulses in grey and a number of closed bifurcation curves[1] of symmetric 2-pulses in green and blue. We can see that the branches of 2-pulses follow the double helix very closely but that all bifurcation curves belonging to 2-pulses are isolas of figure-eight type. As indicated in Fig. 2, we found a family of stacked isolas that differ by the widths of each of the pulses that form the associated 2-pulse profiles. If we fix the width of each pulse, then we found a family of nested isolas that are parametrized by a discrete set of increasing separation distances between the two pulses. We often encountered isolas that initially appeared to contain more fold bifurcations than present in a single figure-eight isola, but these isolas were found to break up into several figure-eight isolas once the step size of the continuation scheme was decreased sufficiently. This observation was also made independently in the recent work [6].

One can think of 2-pulses as being composed of two pulses that both mirror the behaviour of the symmetric and non-symmetric pulses along the parts of the original double helix that are closest to the isola. It is interesting to note that, along each rung, there are two non-symmetric 1-pulses that are related by symmetry. In particular, we can create two different symmetric 2-pulses along the rungs by forming a 2-pulse from each of the two non-symmetric 1-pulses. This is further illustrated in Fig. 3. As shown there, we found two different types of 2-pulses that can be characterised as follows. In the center $x = 0$ of each 2-pulse with profile $U(x)$, we have $U_x(0) = U_{xxx}(0) = 0$. If $x = 0$ corresponds to a positive maximum or a negative minimum of the profile, then the solution behaves

---

[1] Plotted are the L^2-norm of 1-pulses and half the L^2-norm of 2-pulses to make a comparison meaningful.
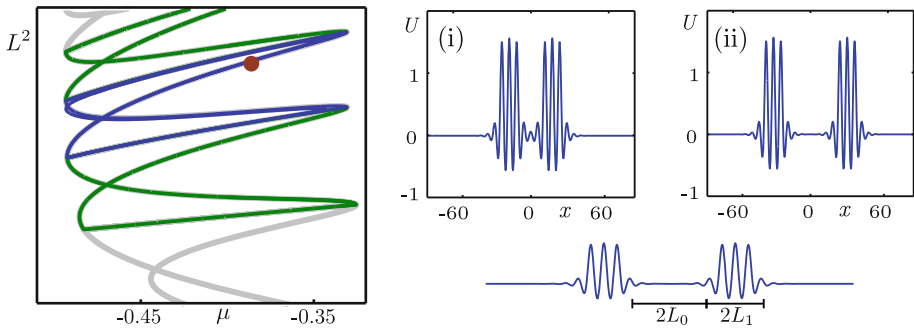
Fig. 2 Plotted are numerically computed figure-eight isolas associated with 2-homoclinic orbits of the Swift–Hohenberg equation (1.1). If we fix the separation distance $2L_0$ between the two pulses, we find a family of stacked isolas whose solution profiles differ by the width $2L_1$ of each individual pulse. If we fix the width of each pulse, we find a family of nested isolas whose profiles differ by the separation distance between the two pulses as illustrated by the profiles in panels (**i**, **ii**) that lie on two different isolas near the bullet in the *left panel*
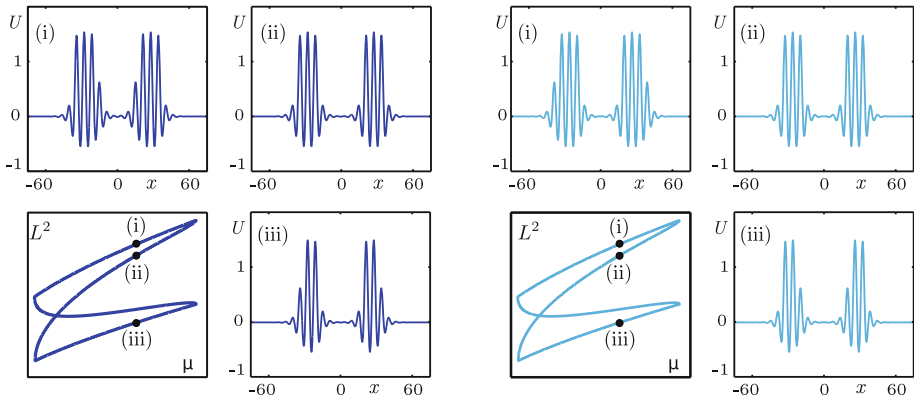

Fig. 3 Shown are numerical computations of two different types of 2-pulse solutions that differ by whether their central point is a positive maximum or negative minimum (*left panels*) or a negative maximum or positive minimum (*right panels*)

as shown in the left panels in Fig. 3. On the other hand, the behaviour will be as shown in the right panels in Fig. 3 if the center $x = 0$ is a negative maximum or a positive minimum of the solution profile. The existence of these different types of 2-homoclinic orbits is a typical phenomenon, as the analysis in [8] shows in a slightly different context.

In this paper, we will refine these results and put them on an analytic footing. We will show that the isolas of figure-eight type are the only possible bifurcation curves for symmetric 2-homoclinic orbits provided that the width of the pulses is sufficiently large and that they are sufficiently well separated. Our analysis follows the approach in [2]. In Sect. 2, we present our assumptions, which are slightly more restrictive than those in [2], and our main results. The existence analysis of 2-pulses is then carried out in Sect. 3. In Sect. 4, we give a geometric interpretation of our results and outline generalizations to non-symmetric 2-pulses and, more generally, to N-pulses.

2 Existence results for 2-pulses

We consider four-dimensional systems

$$u_x = f(u, \mu), \quad u \in \mathbb{R}^4, \ \mu \in \mathbb{R}, \tag{2.1}$$

where f will be a smooth vector field. We shall assume that (2.1) possesses a heteroclinic cycle between the equilibrium $u = 0$ and a periodic orbit, and are interested in locating homoclinic orbits near this cycle.

Firstly, however, let us specify the general properties of the vector field f. We require that (2.1) is both reversible and Hamiltonian. More precisely, we assume the following.

Hypothesis (H1) There exists a linear map $\mathcal{R} : \mathbb{R}^4 \to \mathbb{R}^4$ with $\mathcal{R}^2 = 1$ and $\dim \mathrm{Fix}(\mathcal{R}) = 2$ so that $f(\mathcal{R}u, \mu) = -\mathcal{R}f(u, \mu)$ for all (u, μ).

Reversibility as encoded in Hypothesis (H1) implies that $\mathcal{R}u(-x)$ satisfies (2.1) whenever $u(x)$ does. Solutions with $u(0) \in \mathrm{Fix}(\mathcal{R}) := \{u \in \mathbb{R}^4 : \mathcal{R}u = u\}$ are said to be symmetric as they satisfy $u(x) = \mathcal{R}u(-x)$ for all x.

Hypothesis (H2) There exists a smooth function $\mathcal{H} : \mathbb{R}^4 \times \mathbb{R} \to \mathbb{R}$ with $\mathcal{H}(\mathcal{R}u, \mu) = \mathcal{H}(u, \mu)$, such that

$$f(u, \mu) = \mathcal{J}\mathcal{H}_u(u, \mu), \quad \mathcal{J} = \begin{pmatrix} 0 & -1 \\ 1 & 0 \end{pmatrix},$$

and $\mathcal{H}(0, \mu) = 0$ for all μ.

Next, we introduce the solutions of (2.1) that we will consider. We shall assume that there is a compact interval $J \subset \mathbb{R}$ with nonempty interior $\mathring{J}$ such that the following hypotheses are met for $\mu \in J$.

Hypothesis (H3) The origin $u = 0$ is a saddle-focus of (2.1) for all $\mu \in J$, that is, the linearised vector field has a quadruplet of complex conjugate eigenvalues so that there is a constant $\kappa > 0$ with

$$\mathrm{spec}\,(f_u(0, \mu)) = \{\pm\alpha_0(\mu) \pm \mathrm{i}\beta_0(\mu)\}$$

and $\alpha_0(\mu), \beta_0(\mu) \geq \kappa > 0$ for all $\mu \in J$.

Hypothesis (H4) We assume that (2.1) has, for each $\mu \in J$, a periodic orbit $\gamma(x, \mu)$ with minimal period 2π which satisfy the following for each $\mu \in J$:

(i)   The family $\gamma(x, \mu)$ depends smoothly on μ.
(ii) $\gamma(x, \mu)$ is symmetric with $\gamma(0, \mu) \in \mathrm{Fix}(\mathcal{R})$.
(iii) $\mathcal{H}(\gamma(x, \mu), \mu) = 0$ and $\mathcal{H}_u(\gamma(x, \mu), \mu) \neq 0$ for all $x \in \mathbb{R}$.
(iv) $\gamma(x, \mu)$ has two positive Floquet multipliers $\mathrm{e}^{\pm 2\alpha_1(\mu)}$ with $\alpha_1(\mu) \geq \kappa > 0$ uniformly in $\mu \in J$.

Reversibility implies that both the spectrum of $u = 0$ and the set of characteristic exponents of $\gamma(x, \mu)$ are symmetric under multiplication by -1. Furthermore, the Hamiltonian property of (2.1) allows us to restrict the search for connecting orbits to the zero level set of $\mathcal{H}$.

The above setting fits into the context of [2]. Indeed, Hypotheses (H2) and (H3) are more restrictive than the corresponding assumptions made in [2], where we assumed only that f has a first integral and that the equilibrium $u = 0$ is hyperbolic without assuming anything else about its eigenvalues. We now recall the following result from [2].

Lemma 2.1 ([2]) *Assume that Hypotheses (H1)–(H4) are met, then there exist a $\delta > 0$, a smooth reversible change of coordinates near $\gamma(\cdot, \mu)$, and smooth real-valued functions h^c, h^s_j and h^u_j with $j = 1, 2$ so that (2.1) restricted to the zero level set of $\mathcal{H}$ is, for all $\mu \in J$, of the form*

$$
\begin{aligned}
v^c_x &= 1 + h^c(v, \mu) v^s v^u \\
v^s_x &= -[\alpha_1(\mu) + h^s_1(v, \mu) v^s + h^s_2(v, \mu) v^u] v^s \\
v^u_x &= [\alpha_1(\mu) + h^u_1(v, \mu) v^s + h^u_2(v, \mu) v^u] v^u,
\end{aligned}
\tag{2.2}
$$

where $v = (v^c, v^s, v^u) \in S^1 \times I \times I$ with $I = [-\delta, \delta]$. The reverser $\mathcal{R}$ acts on v via $\mathcal{R}(v^c, v^s, v^u) = (-v^c, v^u, v^s)$.

The dynamics we are interested in is organised by heteroclinic cycles that connect the equilibrium $u = 0$ and the periodic orbit γ. The underlying heteroclinic orbits correspond to intersections of the stable manifold $W^s(0, \mu)$ of the equilibrium $u = 0$ and the strong unstable fibres $W^{uu}(\gamma(\varphi, \mu), \mu)$ of the periodic orbit γ. To capture these intersections, we define the sections

$$
\Sigma^{in}_1 := S^1 \times \{v^s = \delta\} \times I, \quad \Sigma^{out}_1 := S^1 \times I \times \{v^u = \delta\}
$$

in the Fenichel coordinates of Lemma 2.1 near the periodic orbit $\gamma(\cdot, \mu)$ in the zero level set of $\mathcal{H}$ and set

$$
\Gamma := \left\{ (\varphi, \mu) \in S^1 \times J : W^s(0, \mu) \cap W^{uu}(\gamma(\varphi, \mu), \mu) \cap \Sigma^{out}_1 \neq \emptyset \right\}.
\tag{2.3}
$$

We now state two hypotheses that encapsulate the geometric assumptions we impose on the set Γ and the various invariant manifolds introduced above. These hypotheses are illustrated in Figs. 4 and 5 and will be motivated in more detail below. First, we assume that Γ is the graph of a function that maps S^1 into $\mathring{J}$.

Hypothesis (H5) The set Γ is the graph of a smooth function $z : S^1 \to \mathring{J}$. Furthermore, we assume that $z'(\varphi) = 0$ if and only if $\varphi \in \{\ell_m, \ell_M\}$ and that $z''(\ell_{m,M}) \neq 0$. In other words, z has precisely two critical points, namely a minimum and a maximum, which are both nondegenerate.

Thus, we assume that the stable manifold $W^s(0, \mu)$ intersects the strong unstable fiber of $\gamma(\varphi)$ in the section Σ^{out}_1 if, and only if, $\mu = z(\varphi)$. Hypothesis (H5) also assumes that the function $z(\varphi)$ has the shape shown in Fig. 5. Specifically, heteroclinic orbits between $u = 0$ and the periodic orbit γ are created and destroyed in two saddle-node bifurcations that occur when $\mu = z(\varphi)$ with $\varphi = \ell_{m,M}$. Hypothesis (H5) can be relaxed considerably, and we will discuss this in detail in Sect. 4.
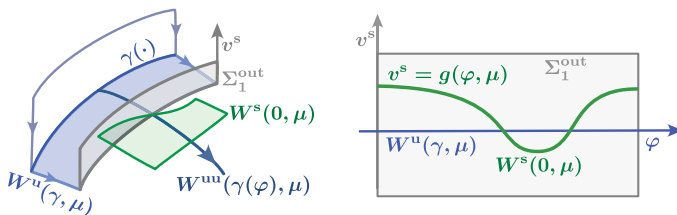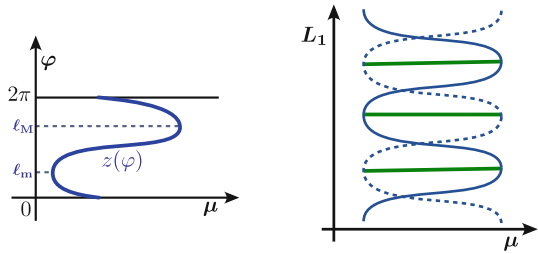

Fig. 4 The geometry of the stable manifold $W^s(0, \mu)$, the unstable manifold $W^u(\gamma, \mu)$ and the strong unstable fibers $W^{uu}(\gamma(\varphi), \mu)$ that we assumed in Hypotheses (H5)–(H6) is illustrated

Fig. 5 Shown are the function $\mu = z(\varphi)$ and the snaking diagram of symmetric 1-homoclinic orbits

Hypothesis (H6) There exist a constant $\eta > 0$ and a smooth function $g : S^1 \times J \to I$ so that

$$W^s(0, \mu) \cap \Sigma_1^{\text{out}} = \{(v^c, v^s, v^u) = (\varphi, g(\varphi, \mu), \delta) : \varphi \in S^1\}$$

for each $\mu \in J$ and $|g_\mu(\varphi, \mu)| \geq \eta > 0$ for all (φ, μ).

Hypothesis (H6) makes two different assumptions. First, we assume that the parameter μ moves the stable manifold $W^s(0, \mu)$ up and down in a monotonic fashion relative to the unstable manifold $W^u(\gamma(\cdot, \mu), \mu)$ of the periodic orbit. This assumption is satisfied, for instance, for near-integrable systems such as the normal form of a Hamiltonian–Hopf bifurcation, which corresponds to a Turing bifurcation of the underlying partial differential equations; see [25] and the references therein. The second assumption in Hypothesis (H6) is that $W^s(0, \mu)$ is a graph over $W^u(\gamma(\cdot, \mu), \mu)$ inside the section Σ_1^{out}. In particular, we assume that the manifold $W^s(0, \mu)$ intersects the section Σ_1^{out} along a circle for all $\mu \in J$. This assumption can be relaxed, and we refer to Sect. 4 for details.

Note that the definition of Γ in (2.3) and Hypotheses (H5)–(H6) imply that

$$g(\varphi, \mu) = 0 \iff \mu = z(\varphi). \tag{2.4}$$

If Hypotheses (H1)–(H6) are met, then (2.1) exhibits homoclinic snaking. More precisely, it was shown in [2] that there are constants $\kappa > 0$, $L_* \gg 1$, and functions $\mu_*(L_1, \varphi)$ and $Z_0(L_1, \varphi)$ with

$$\mu_*(L_1, \varphi) = z(L_1 + \varphi) + \mathrm{O}\left(\mathrm{e}^{-\kappa L_1}\right),$$

$$Z_0(L_1, \varphi) = z(L_1 + \varphi) - z(L_1 - \varphi) + \mathrm{O}\left(\mathrm{e}^{-\kappa L_1}\right), \quad L \geq L_*$$

and $Z_0(L_1, -\varphi) = -Z_0(L_1, \varphi)$ such that the following holds. Equation 2.1 has a symmetric 1-homoclinic orbit to the origin that spends time $2L_1$ near the periodic orbit precisely when $\mu = \mu_*(L_1, 0)$ or $\mu = \mu_*(L_1, \pi)$; see Fig. 5 for an illustration. Furthermore, non-symmetric 1-homoclinic orbits exist precisely when $\mu = \mu_*(L_1, \varphi)$ and $Z_0(L_1, \varphi) = 0$, and it is not difficult to see that this gives the horizontal rungs curves that connect the two snaking curves shown in Fig. 5; we refer to [2] for further details. In particular, given that we know the function $\mu_*(L_1, \varphi)$, the information about both symmetric and non-symmetric 1-homoclinic orbits is contained in the function $Z_0(L_1, \varphi)$ or, more precisely, in its zero level set Z_0^{-1} in the (φ, L_1)-plane. This is illustrated further in Fig. 6, which contains the vertical lines $\varphi = 0$ and $\varphi = \pi$ in Z_0^{-1} as well as the connecting rungs curves corresponding to non-symmetric 1-pulses that emerge via pitchfork bifurcations from symmetric 1-pulses at the discrete set

$$L_1 = L_i^\varphi(n) = \ell_i + \varphi + 2\pi n + \mathrm{O}(\mathrm{e}^{-\kappa n}), \quad i = \mathrm{m, M}, \ \varphi \in \{0, \pi\}, \ n \geq n_*$$
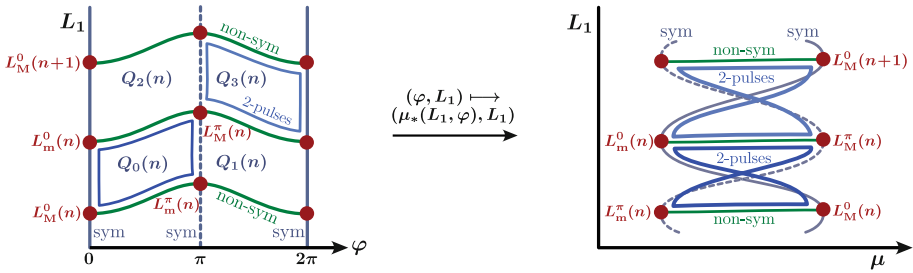
Fig. 6 The bifurcation curves of symmetric (labelled sym) and non-symmetric (labelled non-sym) 1-homoclinic orbits are shown in the (φ, L_1) and the (μ, L_1)-planes. Non-symmetric 1-pulses bifurcate from symmetric 1-pulses at the pitchfork bifurcation points shown as *bullets*. Symmetric 2-homoclinic orbits exist on isolas near the original *snaking curves*

of bifurcation points. Recall here that ℓ_m and ℓ_M correspond, respectively, to the minimum and maximum of the function $z(\varphi)$. For each fixed n, the set Z_0^{-1} encloses precisely four open rectangular sets that we denote by $Q_j(n)$ with $j = 0, \ldots, 3$. We can now state our result on the existence of 2-homoclinic orbits.

Theorem 1 *Assume that Hypotheses* (H1)–(H6) *are met. There exist integers $m_*, n_* \gg 1$ such that, for each pair (m, n) of integers with $m \geq m_*$ and $n \geq n_*$, there are precisely two closed curves without self-intersection inside each rectangular set $Q_j(n)$ with $j = 0, \ldots, 3$ along which 2-homoclinic orbits with width $L_1 \approx n$ and separation distance $L_0 \approx m$ exist. Furthermore, for each fixed n, these curves converge in the symmetric Hausdorff distance to the boundaries of the sets $Q_j(n)$ as $m \to \infty$.*

The theorem is vague on how the integers m and n relate to the transition times L_0 and L_1. Roughly speaking, n measures how many times the 2-homoclinic orbits winds around the periodic orbit, while m measures how many times the 2-homoclinic orbit winds around the equilibrium during its passage near $u = 0$: recall that we assumed that $u = 0$ is a bi-focus. The precise relation between (m, n) and (L_0, L_1) will become clear during the proof in Sect. 3.

For each fixed pair (m, n), there are four symmetric 2-pulse isolas in the union $Q_0(n) \cup Q_1(n)$. As we shall see in the course of the proof, the profiles of the associated symmetric 2-pulses along these four isolas differ in the following way. For $j = 1, \ldots, 4$, let $u^{(j)}(0) \in \text{Fix}(\mathcal{R})$ denotes the value of the symmetric 2-pulse on the jth isola at its point of symmetry, then $u^{(j)}(0)$ lies in the jth quadrant of the two-dimensional space $\text{Fix}(\mathcal{R})$ upon ordering the four isolas appropriately and choosing an appropriate coordinate system in $\text{Fix}(\mathcal{R})$. In particular, for the Swift–Hohenberg equation, we can take (U, U_{xx}) as the coordinates in $\text{Fix}(\mathcal{R})$, so that $x = 0$ corresponds to a positive or negative maximum or a positive or negative minimum of the profile $U(x)$ along the four isolas. An analogous statement is true for the four isolas in the set $Q_2(n) \cup Q_3(n)$.

3 Bifurcation equations for symmetric 2-pulses

We are interested in constructing symmetric 2-homoclinic orbits to the equilibrium $u = 0$ that remain for a prescribed time $2L_0$ near the equilibrium $u = 0$ and for $2L_1$ time units near the periodic orbit $\gamma(\cdot, \mu)$. Our strategy for finding 2-pulses is illustrated in Fig. 7 and will now be
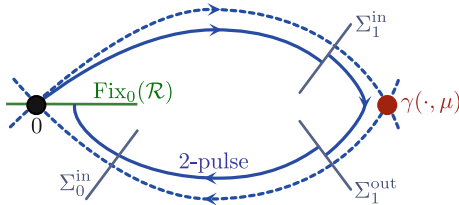
Fig. 7 Illustrated are the underlying heteroclinic cycle between $u = 0$ and the periodic orbit γ, the location of the various sections we shall use, the fixed-point space $\mathrm{Fix}_0(\mathcal{R})$ near $u = 0$, and three solution pieces that we match together to construct 2-pulses

outlined in more detail. Let $\mathrm{Fix}_0(\mathcal{R})$ be the fixed-point space of $\mathcal{R}$ restricted to some neighborhood of the equilibrium $u = 0$, and denote by $\mathrm{Fix}_1^{\mathrm{out}}(\mathcal{R})$ the pull-back of $\mathrm{Fix}_0(\mathcal{R})$ to the section Σ_1^{out} under the flow. Symmetric 2-homoclinic orbits then correspond to intersections of $\mathrm{Fix}_1^{\mathrm{out}}(\mathcal{R})$ with the unstable manifold $W^u(0, \mu)$ of the equilibrium $u = 0$ tracked through a neighborhood of the periodic orbit $\gamma(\cdot, \mu)$. We will prove that $\mathrm{Fix}_1^{\mathrm{out}}(\mathcal{R})$ is C^1-close to the stable manifold $W^s(0, \mu)$ of $u = 0$. As we shall see, this property implies that the bifurcation equations for symmetric 2-homoclinic orbits can be viewed as symmetry-breaking perturbations of the bifurcation equations for 1-homoclinic orbits. An essential feature is that these perturbations do not change sign, which will imply that symmetric 2-homoclinic orbits exist along closed curves in the (φ, L)-plane as illustrated in Fig. 6. On a technical level, we use a smooth, reversible, symplectic transformation into normal form to capture the dynamics near $u = 0$, while we shall use the Fenichel coordinates from Lemma 2.1 to track solutions as they pass near the periodic orbit.

3.1 Dynamics near the origin

We first consider the local dynamics near $u = 0$. Hypotheses (H1)–(H3) together with the results in [3,19,20] imply that there is a smooth reversible symplectic coordinate transformation from $u \in \mathbb{R}^4$ to new coordinates $(p, q) \in \mathbb{R}^2 \times \mathbb{R}^2$ with $p = (p_1, p_2)$ and $q = (q_1, q_2)$ such that the Hamiltonian $\mathcal{H}$ in the new variables is given by

$$\mathcal{H}(p, q, \mu) = \tilde{\mathcal{H}}(\iota, \mu) = \alpha_0(\mu)\iota_1 + \beta_0(\mu)\iota_2 + \mathrm{O}(|\iota|^2),$$

where

$$\iota_1 = p_1 q_1 + p_2 q_2, \quad \iota_2 = p_1 q_2 - p_2 q_1$$

are invariants, while the reverser $\mathcal{R}$ is given by

$$\mathcal{R}(p_1, p_2, q_1, q_2) = (q_2, q_1, p_2, p_1).$$

Using the above normal form of the Hamiltonian and the symplectic form $\mathcal{J}$, we see that the differential equation near $u = 0$ becomes

$$p_x = \left[\begin{pmatrix} -\alpha_0(\mu) & \beta_0(\mu) \\ -\beta_0(\mu) & -\alpha_0(\mu) \end{pmatrix} + \mathrm{O}(|\iota|) \right] p, \quad q_x = \left[\begin{pmatrix} \alpha_0(\mu) & \beta_0(\mu) \\ -\beta_0(\mu) & \alpha_0(\mu) \end{pmatrix} + \mathrm{O}(|\iota|) \right] q.$$

In particular, the local stable manifold $W^s(0, \mu)$ of $u = 0$ is given by $W^s(0, \mu) = \{(p, 0) : p \text{ near zero}\}$. Alternatively, we can use the polar coordinates $p = re^{i\phi}$ and the invariants $\iota \in \mathbb{R}^2$ to write the differential equation near $(p, q) = 0$ as

$$r_x = -\tilde{\mathcal{H}}_{\iota_1}(\iota, \mu)r = -[\alpha_0(\mu) + O(\iota)]r$$
$$\phi_x = -\tilde{\mathcal{H}}_{\iota_2}(\iota, \mu) = -\beta_0(\mu) + O(\iota) \tag{3.1}$$
$$\iota_x = 0.$$

Our first aim is to define a transverse section Σ_0^{in} centered at $r = \delta$ inside $\mathcal{H}^{-1}(0)$. First, the zero level set of $\mathcal{H}$ is determined by

$$\mathcal{H}(p, q, \mu) = \tilde{\mathcal{H}}(\iota, \mu) = \alpha_0(\mu)\iota_1 + \beta_0(\mu)\iota_2 + O(|\iota|^2) = 0,$$

which can be solved uniquely for ι_1 as a function of (ι_2, μ) to get

$$\iota_1 = \iota_1^*(\iota_2, \mu) = -\frac{\beta_0(\mu)}{\alpha_0(\mu)}\iota_2 + O(|\iota_2|^2).$$

The desired two-dimensional section Σ_0^{in} inside the zero level set of $\mathcal{H}$ is now given by

$$\Sigma_0^{in} := \left\{(r, \phi, \iota_1, \iota_2) = (\delta, \phi, \iota_1^*(\iota_2, \mu), \iota_2) : (\phi, \iota_2) \in S^1 \times I_0\right\}$$

with $\mu \in J$, where I_0 is a sufficiently small open interval that contains zero. Next, we consider the fixed-point space $\text{Fix}_0(\mathcal{R})$ of the reverser near the origin. In the new variables (r, ϕ, ι), we have

$$\text{Fix}_0(\mathcal{R}) = \left\{(p, q) : q = (p_2, p_1), \ p \in \mathbb{R}^2\right\}$$
$$= \left\{(r, \phi, \iota) : \iota = (2p_1p_2, p_1^2 - p_2^2) = r^2(\sin 2\phi, \cos 2\phi)\right\}.$$

Solving

$$\iota_1 = \iota_1^*(\iota_2, \mu), \quad \iota = r^2(\sin 2\phi, \cos 2\phi),$$

for ϕ as a function of (r, μ), we obtain four solution branches given by

$$\phi = \phi_j^*(r, \mu) = \phi_j^*(\mu) + O(r^2), \quad j = 0, \dots, 3,$$

where

$$\phi_j^*(\mu) := \phi^*(\mu) + \frac{j\pi}{2}, \quad \phi^*(\mu) := -\frac{1}{2}\arctan\frac{\beta_0(\mu)}{\alpha_0(\mu)} \in \left(\frac{\pi}{4}, \frac{\pi}{2}\right)$$

for $j = 0, \dots, 3$. In particular, we have

$$\text{Fix}_0(\mathcal{R}) \cap \mathcal{H}^{-1}(0) =$$
$$\bigcup_{j=0,\dots,3} \left\{(r, \phi, \iota) : \iota = r^2(\sin 2\phi_j^*(r, \mu), \cos 2\phi_j^*(r, \mu)), \phi = \phi_j^*(r, \mu), 0 \leq r \leq r_0\right\}.$$

Note that the curves associated with $j = 0, \dots, 3$ lie in the $(j + 1)$th quadrant of the two-dimensional fixed-point space $\text{Fix}(\mathcal{R})$. We now pull these curves back until they intersect the section Σ_0^{in} that we defined above.

Lemma 3.1 *The pull-back* $\text{Fix}_0^{in}(\mathcal{R})$ *of* $\text{Fix}_0(\mathcal{R}) \cap \mathcal{H}^{-1}(0)$ *under the flow to the section* Σ_0^{in} *is the union of the four curves*

$$(\phi, \iota_2) = (\tilde{\phi}_j^*, \tilde{\iota}_j^*)(L_0, \mu), \quad L_0 \gg 1, \quad \mu \in J$$

with

$$\tilde{\phi}_j^*(L_0, \mu) = \phi_j^*(\mu) + \beta_0(\mu)L_0 + O(L_0 e^{-2\alpha_0(\mu)L_0})$$
$$\tilde{\iota}_j^*(L_0, \mu) = \delta^2 \cos(2\phi_j^*(\mu))e^{-2\alpha_0(\mu)L_0}\left[1 + O(e^{-2\alpha_0(\mu)L_0})\right],$$

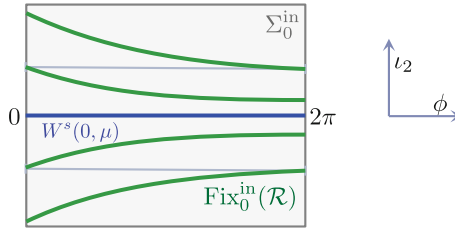**Fig. 8** Shown are two of the four curves whose union is the pull-back $\mathrm{Fix}_0^{\mathrm{in}}(\mathcal{R})$ of $\mathrm{Fix}_0(\mathcal{R})$ in the section Σ_0^{in} that is parametrized by $(\varphi, \iota_2 \in S^1 \times I)$. Note that the section is a cylinder, so that the vertical lines $\varphi = 0$ and $\varphi = 2\pi$ are identified, and that $\iota_2 = 0$ corresponds to the stable manifold $W^s(0, \mu)$

for $j = 0, \ldots, 3$, where $L_0 \gg 1$ denotes the time needed for the associated solution to go from Σ_0^{in} to $\mathrm{Fix}_0(\mathcal{R})$.

Since

$$W_{\mathrm{loc}}^s(0, \mu) \cap \Sigma_0^{\mathrm{in}} = \{(r, \phi, \iota) = (\delta, \phi, 0, 0) : \phi \in S^1\},$$

we see that the set $\mathrm{Fix}_0^{\mathrm{in}}(\mathcal{R})$, which is parametrized by L_0, is pointwise $\mathrm{O}(L_0 e^{-2\alpha_0(\mu)L_0})$-close to $W_{\mathrm{loc}}^s(0, \mu)$, and we refer to Fig. 8 for an illustration of the geometry.

Proof Recall from (3.1) that $\iota(x) = \iota$ is independent of x. We require that $(r(L_0), \phi(L_0), \iota) \in \mathrm{Fix}_0(\mathcal{R} \cap \mathcal{H}^{-1}(0))$, which gives

$$\iota = r(L_0)^2(\sin 2\phi(L_0), \cos 2\phi(L_0)), \quad \phi(L_0) = \phi_j^*(\mu) + \mathrm{O}(r(L_0)^2). \tag{3.2}$$

Next, we solve (3.1) with $r(0) = \delta$ to get

$$r(x) = \delta e^{-[\alpha_0(\mu) + \mathrm{O}(r(L_0)^2)]x}, \quad \phi(x) = \phi(0) - [\beta_0(\mu) + \mathrm{O}(r(L_0)^2)]x$$

for $0 \leq x \leq L_0$. Thus, we obtain

$$r(L_0) = \delta e^{-\alpha_0(\mu)L_0} \left[1 + \mathrm{O}(e^{-2\alpha_0(\mu)L_0})\right]$$

and therefore

$$\phi(L_0) = \phi(0) - [\beta_0(\mu) + \mathrm{O}(e^{-2\alpha_0(\mu)L_0})]L_0.$$

The condition (3.2) gives

$$\phi(0) = \phi_j^*(\mu) + \beta_0(\mu)L_0 + \mathrm{O}(L_0 e^{-2\alpha_0(\mu)L_0}),$$

and the assertions in the lemma follow now easily. □

3.2 The transition map from Σ_0^{in} to Σ_1^{out}

Our goal is to characterise the pull-back $\mathrm{Fix}_1^{\mathrm{out}}(\mathcal{R}) \subset \Sigma_1^{\mathrm{out}}$ of the set $\mathrm{Fix}_0^{\mathrm{in}}(\mathcal{R})$ under the flow. Hypothesis (H6) implies that the transition map

$$\mathcal{T}: \quad \Sigma_0^{\mathrm{in}} \longrightarrow \Sigma_1^{\mathrm{out}}$$

that is induced by the backward flow can be written as

$$(v^c, v^s) = \mathcal{T}(\phi, \iota_2, \mu) = \left(\varphi^*(\phi, \mu), g(\varphi^*(\phi, \mu), \mu)\right) + b(\phi, \iota_2, \mu)\iota_2,$$
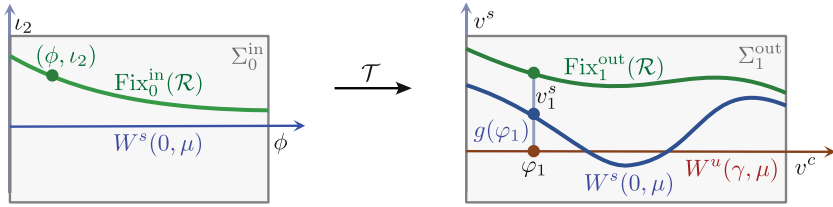
Fig. 9 Illustrated is the action of $\mathcal{T}$ on $\mathrm{Fix}_0^{\mathrm{in}}(\mathcal{R})$ and the interpretation of the decomposition $\mathcal{T}(\phi, \iota_2, \mu) = (\varphi_1, g(\varphi_1, \mu) + v_1^s)$

where $b(\varphi, \iota_2, \mu)$ is smooth. The map $\varphi^*(\cdot, \mu) : S^1 \to S^1$ is a diffeomorphism for each $\mu \in J$ and can therefore be written as

$$\varphi^*(\phi, \mu) = \sigma[\phi + a(\phi, \mu)], \tag{3.3}$$

where $\sigma = \pm 1$ indicates whether the diffeomorphism $\varphi^*(\cdot, \mu)$ preserves orientation or not and where $a(\phi, \mu)$ is 2π-periodic in ϕ with $a_\phi(\phi, \mu) > -1$ for all (ϕ, μ). It will be convenient to put the transition map into the form

$$(\varphi_1, g(\varphi_1, \mu) + v_1^s) = \mathcal{T}(\phi, \iota_2, \mu)$$

for appropriate values of (φ_1, v_1^s); see Fig. 9. Writing $b = (b^c, b^s)$, we find that

$$\varphi_1 = \varphi^*(\phi, \mu) + b^c(\phi, \iota_2, \mu)\iota_2$$

and

$$
\begin{aligned}
v_1^s &= g(\varphi^*(\phi, \mu), \mu) + b^s(\phi, \iota_2, \mu)\iota_2 - g(\varphi_1, \mu) \\
&= g(\varphi^*(\phi, \mu), \mu) - g(\varphi^*(\phi, \mu) + b^c(\phi, \iota_2, \mu)\iota_2, \mu) + b^s(\phi, \iota_2, \mu)\iota_2 \\
&= -g_\varphi(\varphi^*(\phi, \mu), \mu)b^c(\phi, \iota_2, \mu)\iota_2 + O(|\iota_2|^2) + b^s(\phi, \iota_2, \mu)\iota_2 \\
&= \left[b^s(\phi, 0, \mu) - g_\varphi(\varphi^*(\phi, \mu), \mu)b^c(\phi, 0, \mu) + O(|\iota_2|) \right] \iota_2 \\
&= [d(\phi, \mu) + O(|\iota_2|)] \iota_2,
\end{aligned}
$$

where

$$d(\phi, \mu) := \frac{\det D_{(\phi, \iota_2)} \mathcal{T}(\phi, 0, \mu)}{D_\phi \varphi^*(\phi, \mu)}$$

is 2π-periodic in ϕ with $|d(\phi, \mu)| \geq \eta > 0$ for $(\phi, \mu) \in S^1 \times J$.

Lemma 3.1 shows that the set $\mathrm{Fix}_0^{\mathrm{in}}(\mathcal{R}) \subset \Sigma_0^{\mathrm{in}}$, in whose image under $\mathcal{T}$ we are interested, consists of the four curves

$$\phi = \tilde{\phi}_j^*(L_0, \mu) = \phi_j^*(\mu) + \beta_0(\mu)L_0 + O(L_0 e^{-2\alpha_0(\mu)L_0})$$

$$\iota_2 = \tilde{\iota}_j^*(L_0, \mu) = \delta^2 \cos(2\phi_j^*(\mu))e^{-2\alpha_0(\mu)L_0} \left[1 + O(e^{-2\alpha_0(\mu)L_0}) \right]$$

with $j = 0, \ldots, 3$, where $L_0 \gg 1$ and $\mu \in J$. Substituting this parametrization of $\mathrm{Fix}_0^{\mathrm{in}}(\mathcal{R})$ into the expression for (φ_1, v_1^s) and using (3.3), we obtain that the pull-back $\mathrm{Fix}_1^{\mathrm{out}}(\mathcal{R}) \subset \Sigma_1^{\mathrm{out}}$ is given by

$$\mathrm{Fix}_1^{\mathrm{out}}(\mathcal{R}): \quad (v^c, v^u) = (\varphi_1, g(\varphi_1, \mu) + v_1^s) \tag{3.4}$$

with

$$\varphi_1 = \varphi_1(L_0, \mu) = \varphi^*(\phi, \mu) + b^c(\phi, \iota_2, \mu)\iota_2$$
$$= \sigma \left[\phi_j^*(\mu) + \beta_0(\mu)L_0 + a(\phi_j^*(\mu) + \beta_0(\mu)L_0, \mu) + O(L_0 e^{-2\alpha_0(\mu)L_0}) \right] \quad (3.5)$$

$$v_1^s = v_1^s(L_0, \mu) = [d(\phi, \mu) + O(|\iota_2|)] \iota_2$$
$$= \delta^2 \cos(2\phi_j^*(\mu)) \underbrace{\left[d(\sigma(\phi_j^*(\mu) + \beta_0(\mu)L_0), \mu) + O(L_0 e^{-2\alpha_0(\mu)L_0}) \right]}_{=:d_j(L_0, \mu)} e^{-2\alpha_0(\mu)L_0}, \quad (3.6)$$

where $|d_j(L_0, \mu)| \geq \eta > 0$ uniformly in $L_0 \gg 1$ and $\mu \in J$.

3.3 Matching near the periodic orbit

Using the results obtained above, the problem of finding symmetric 2-homoclinic orbits of (2.1) is now equivalent to finding solutions $v(x)$ of (2.2) in $S^1 \times I \times I$ that satisfy

$$v(-L_1) \in W^u(0, \mu) \cap \Sigma_1^{\text{in}}, \quad v(L_1) \in \text{Fix}_1^{\text{out}}(\mathcal{R}) \subset \Sigma_1^{\text{out}} \quad (3.7)$$

for some $L_1 \gg 1$. The next lemma gives a detailed description of solutions that stay near the periodic orbit for sufficiently large prescribed times.

Lemma 3.2 [2] *There exist positive constants L_* and κ so that the following is true: For each $L_1 > L_*, \varphi \in S^1$ and $\mu \in J$, there is a unique solution $v(x)$, also referred to as $v(x, \varphi, \mu)$, of (2.2) that is defined for $x \in [-L_1, L_1]$ and satisfies*

$$v(-L_1) \in \Sigma_1^{\text{in}}, \quad v(L_1) \in \Sigma_1^{\text{out}}, \quad v^c(0) = \varphi, \quad v(x) \in S^1 \times I \times I, \quad \forall x \in [-L_1, L_1].$$

Furthermore, we have

$$v(-L_1) = \left(\varphi - L_1 + O\left(e^{-\kappa L_1}\right), \delta, \delta e^{-2\alpha_1(\mu)L_1} \left(1 + O(e^{-\kappa L_1})\right) \right)$$
$$v(L_1) = \left(\varphi + L_1 + O\left(e^{-\kappa L_1}\right), \delta e^{-2\alpha_1(\mu)L_1} \left(1 + O\left(e^{-\kappa L_1}\right)\right), \delta \right)$$
$$v(0) = \left(\varphi, \delta e^{-\alpha_1(\mu)L_1} \left(1 + O\left(e^{-\kappa L_1}\right)\right), \delta e^{-\alpha_1(\mu)L_1} \left(1 + O\left(e^{-\kappa L_1}\right)\right) \right). \quad (3.8)$$

The solution $v(x)$ is smooth in (L_1, φ, μ), and the error estimates in (3.8) can be differentiated. Furthermore, we have

$$v(x, -\varphi, \mu) = \mathcal{R}v(-x, \varphi, \mu), \quad \varphi \in S^1, \quad |x| \leq L_1, \quad \mu \in J. \quad (3.9)$$

In particular, the solution $v(x, \varphi, \mu)$ is $\mathcal{R}$-reversible with $v(0) \in \text{Fix}(\mathcal{R})$ if and only if $\varphi \in \Theta$.

Lemma 3.2 shows that $v(x) = v(x, \varphi, \mu)$ for an appropriate value of $\varphi \in S^1$, while (3.9) implies that $v(-L_1, \varphi, \mu) \in W^u(0, \mu) \cap \Sigma_1^{\text{in}}$ if and only if $v(L_1, -\varphi, \mu) \in W^s(0, \mu) \cap \Sigma_1^{\text{out}}$. Thus, using also Hypothesis (H6) and (3.4)-(3.6), we see that (3.7) is equivalent to

$$v^s(L_1, -\varphi, \mu) = g(v^c(L_1, -\varphi, \mu), \mu)$$
$$v^s(L_1, \varphi, \mu) = g(\varphi_1(L_0, \mu), \mu) + v_1^s(L_0, \mu)$$
$$v^c(L_1, \varphi, \mu) = \varphi_1(L_0, \mu).$$

Instead of this system, we will use the equivalent, but slightly more convenient, formulation

$$v^s(L_1, -\varphi, \mu) = g(v^c(L_1, -\varphi, \mu), \mu) \tag{3.10}$$

$$v^s(L_1, \varphi, \mu) = g(v^c(L_1, \varphi, \mu), \mu) + v_1^s(L_0, \mu) \tag{3.11}$$

$$v^c(L_1, \varphi, \mu) = \varphi_1(L_0, \mu). \tag{3.12}$$

We remark that (φ_1, v_1^s) depends on $j = 0, \ldots, 3$, but we will fix j from now on and omit the dependence on j.

First, we solve (3.10). Using the expansions for (v^c, v^s) from (3.8), the fact (2.4) that $g(\varphi, \mu) = 0$ if and only if $\mu = z(\varphi)$, and the property $|g_\mu(\varphi, \mu)| \geq \eta > 0$ from Hypothesis (H6), we obtain via the implicit function theorem that there is a function $e(L_1, \varphi)$ such that (3.10) holds if and only if

$$\mu = \mu_*(L_1, \varphi) := z(L_1 - \varphi) + e(L_1, -\varphi), \quad e(L_1, \varphi) = O(e^{-\kappa L_1}) \tag{3.13}$$

uniformly in $L_1 \gg 1$ and $\varphi \in S^1$.

Next, consider (3.11) and note that the unique solution of (3.11) with $v_1^s = 0$ is given by $\mu = z(L_1 + \varphi) + e(L_1, \varphi)$. Thus, we set

$$\mu = z(L_1 + \varphi) + e(L_1, \varphi) + \mu_2 =: \mu_1(L_1, \varphi) + \mu_2 \tag{3.14}$$

and consider (3.11) in the form

$$g(v^c(L_1, \varphi, \mu), \mu) - v^s(L_1, \varphi, \mu) + v_1^s(L_0, \mu) = 0,$$

which then becomes

$$g(v^c(L_1, \varphi, \mu_1(L_1, \varphi) + \mu_2), \mu_1(L_1, \varphi) + \mu_2) - v^s(L_1, \varphi, \mu_1(L_1, \varphi) + \mu_2) \tag{3.15}$$

$$+ v_1^s(L_0, \mu_1(L_1, \varphi) + \mu_2) - v_1^s(L_0, \mu_1(L_1, \varphi)) = -v_1^s(L_0, \mu_1(L_1, \varphi)).$$

The preceding discussion shows that the left-hand side vanishes when $\mu_2 = 0$, and (3.15) can therefore be written as

$$\tilde{g}(L_0, L_1, \varphi, \mu_2)\mu_2 = -v_1^s(L_0, \mu_1(L_1, \varphi)), \tag{3.16}$$

where

$$\tilde{g}(L_0, L_1, \varphi, \mu_2) = g_\mu(L_1 + \varphi, z(L_1 + \varphi)) + O(e^{-\kappa L_0} + e^{-\kappa L_1} + |\mu_2|) \tag{3.17}$$

for some positive κ uniformly in $L_0, L_1 \gg 1, \varphi \in S^1$, and $|\mu_2|$ small. Equation 3.6 shows that

$$v_1^s(L_0, \mu_1(L_1, \varphi)) = d_j(L_0, \mu_1(L_1, \varphi))e^{-2\alpha_0(\mu_1(L_1, \varphi))L_0},$$

and we conclude from (3.17) and Hypothesis (H6) that (3.16) has a unique solution $\mu_2 = \mu_2(L_0, L_1, \varphi)$ and that this solution has the expansion

$$\mu_2(L_0, L_1, \varphi) = -\underbrace{\left[\frac{d_j(L_0, z(L_1 + \varphi))}{g_\mu(L_1 + \varphi, z(L_1 + \varphi))} + O(e^{-\kappa L_0} + e^{-\kappa L_1}) \right]}_{=:\tilde{d}_j(L_0, L_1, \varphi)} e^{-2\alpha_0(\mu_1(L_1, \varphi))L_0}.$$

$$\tag{3.18}$$

Note that $\eta_1 \geq |\tilde{d}_j(L_0, L_1, \varphi)| \geq \eta_0 > 0$ and that the derivatives of $\tilde{d}_j$ with respect to any of its arguments are bounded by η_1 uniformly in $L_0, L_1 \gg 1$ and $\varphi \in S^1$.
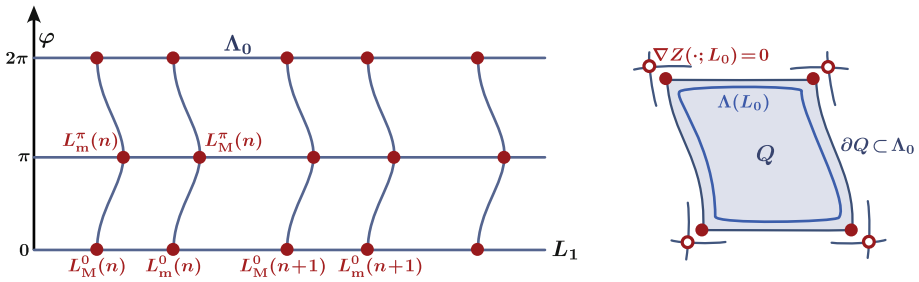
Fig. 10 The *left panel* illustrates the zero level set Λ_0 of the function $Z_0(L_1, \varphi)$ in the cylinder $(L_*, \infty) \times S^1$. The set Λ_0 contains the horizontal lines $\varphi = 0$ and $\varphi = \pi$ as well as infinitely many connecting rung curves that begin and end at the critical points $L_1 = L_{m,M}^{0,\pi}(n)$ along the *horizontal lines*. The *right panel* shows one of the rectangles Q enclosed by Λ_0 together with the critical points and the zero level set $\Lambda(L_0)$ of $Z(\cdot; L_0)$ for fixed L_0

The solution $\mu = \mu_*(L_1, \varphi)$ of (3.10) from (3.13) and the solution $\mu = \mu_1(L_1, \varphi) + \mu_2(L_0, L_1, \varphi)$ of (3.11) from (3.14) and (3.18) need to coincide. Inspecting their expansions, we see that these solutions coincide if and only if

$$
\begin{aligned}
Z(L_1, \varphi; L_0) &:= \mu_1(L_1, \varphi) + \mu_2(L_0, L_1, \varphi) - \mu_*(L_1, \varphi) \\
&= \underbrace{z(L_1 + \varphi) + e(L_1, \varphi) - z(L_1 - \varphi) - e(L_1, -\varphi)}_{=: Z_0(L_1, \varphi)} + \mu_2(L_0, L_1, \varphi) \\
&= 0.
\end{aligned}
\tag{3.19}
$$

Note that $Z_0(L_1, -\varphi) = -Z_0(L_1, \varphi)$ for all (L_1, φ), which implies that $Z_0(L_1, 0) = Z_0(L_1, \pi) = 0$ for all L_1. It was shown in [2] under hypotheses that are weaker than ours that $\Lambda_0 := Z_0^{-1}(0)$ looks as shown in Fig. 10. Furthermore, it was shown there that the critical points of Z_0 in λ_0 are given by (L_1, φ) with $\varphi \in \Theta := \{0, \pi\}$ and $L_1 = \ell_i - \varphi + 2\pi n + O(e^{-\kappa n})$ for $i = m, M$ and integers $n \gg 1$, where we recall that ℓ_m and ℓ_M denote, respectively, the minimum and maximum of the function z. Finally, it follows from Hypothesis (H5) that the critical points of Z_0 in Λ_0 are nondegenerate since their Hessian

$$
D^2 Z_0(L_1, \varphi) = \begin{pmatrix} 0 & 2z''(\ell_i) + O(e^{-\kappa n}) \\ 2z''(\ell_i) + O(e^{-\kappa n}) & 0 \end{pmatrix}, \quad i = m, M
\tag{3.20}
$$

is nondegenerate.

Our goal is to investigate the nature of the zero level set

$$
\Lambda(L_0) := \{(L_1, \varphi) : Z(L_1, \varphi; L_0) = 0\}
$$

of $Z(L_1, \varphi; L_0)$ for each fixed value of $L_0 \gg 1$. Note that μ_2 is exponentially small in L_0 so that Z_0 and $Z(\cdot; L_0)$ are close for each $L_0 \gg 1$, and we therefore expect that $\Lambda(L_0)$ is close to Λ_0. Moreover, using (3.18), we see that, for $(L_1, \varphi) \in \Lambda_0$ and $L_0 \gg 1$, we have

$$
\begin{aligned}
Z(L_1, \varphi; L_0) &= Z_0(L_1, \varphi) + \mu_2(L_0, L_1, \varphi) \\
&= \mu_2(L_0, L_1, \varphi) = \underbrace{\tilde{d}_j(L_0, L_1, \varphi)}_{|\ldots| \geq \eta_0 > 0} e^{-2\alpha_0(\mu_1(L_1, \varphi))L_0} \neq 0 \quad \forall (L_1, \varphi) \in \Lambda_0,
\end{aligned}
$$

so that $\Lambda_0 \cap \Lambda(L_0) = \emptyset$ for all $L_0 \gg 1$. First, we consider the critical points of Z for fixed L_0, which must lie near the critical points of Z_0. Thus, pick one of the critical points (L_1^0, φ^0)

of Z_0 in Λ_0 that we discussed above and write $(L_1, \varphi) = (L_1^0, \varphi^0) + (\tilde{L}, \tilde{\varphi})$. Expanding $Z(L_1, \varphi; L_0)$ in $(\tilde{L}, \tilde{\varphi})$ for fixed L_0 and recalling (3.18) and (3.20), we see that

$$
\begin{aligned}
D_{(L_1,\varphi)}Z(L_1, \varphi; L_0) &= DZ_0(L_1^0 + \tilde{L}, \varphi^0 + \tilde{\varphi}) + D_{(L_1,\varphi)}\mu_2(L_0, L_1^0 + \tilde{L}, \varphi^0 + \tilde{\varphi}) \\
&= D^2 Z_0(L_1^0, \varphi^0)(\tilde{L}, \tilde{\varphi}) \\
&\quad + \mathrm{O}\left((e^{-\kappa L_0} + |\tilde{L}| + |\tilde{\varphi}|)(|\tilde{L}| + |\tilde{\varphi}|)\right) + D_{(L_1,\varphi)}\mu_2(L_0, L_1^0, \varphi^0) \\
&= 0
\end{aligned}
$$

can be solved uniquely for $(\tilde{L}, \tilde{\varphi})$ for each $L_0 \gg 1$ and that this solution satisfies

$$
(\tilde{L}, \tilde{\varphi}) = \mathrm{O}(e^{-2\alpha_0(\mu_1(L_1^0, \varphi^0))L_0}).
$$

Furthermore, the value of $Z(L_1, \varphi; L_0)$ at these L_0-dependent critical points is given by

$$
\begin{aligned}
Z(L_1^0 + \tilde{L}, \varphi^0 + \tilde{\varphi}; L_0) &= \mathrm{O}((|\tilde{L}| + |\tilde{\varphi}|)^2) + \mu_2(L_0, L_1^0 + \tilde{L}, \varphi^0 + \tilde{\varphi}) \\
&= \mu_2(L_0, L_1^0, \varphi^0) + \mathrm{O}\left((e^{-\kappa L_0} + |\tilde{L}| + |\tilde{\varphi}|)(|\tilde{L}| + |\tilde{\varphi}|)\right) \\
&= \tilde{d}_j(L_0, L_1^0, \varphi^0)e^{-2\alpha_0(\mu_1(L_1^0, \varphi^0))L_0} + \mathrm{O}\left(e^{-\kappa L_0}e^{-2\alpha_0(\mu_1(L_1^0, \varphi^0))L_0}\right) \\
&= \underbrace{\left[\tilde{d}_j(L_0, L_1^0, \varphi^0) + \mathrm{O}(e^{-\kappa L_0})\right]}_{|...| \geq \eta > 0} e^{-2\alpha_0(\mu_1(L_1^0, \varphi^0))L_0}
\end{aligned}
$$

uniformly in $L_0 \gg 1$. In particular, the set $\Lambda(L_0)$ does not contain any critical points of $Z(\cdot; L_0)$ and is therefore locally a smooth curve that we can parametrize by its arclength s.

Figure 10 summarizes what we have shown so far. For fixed index j, the quantity μ_2 has a definite sign, and since $\Lambda_0 \cap \Lambda(L_0) = \emptyset$, the associated set $\Lambda(L_0)$ is the disjoint union of sets that each lie strictly inside one of the bounded rectangles whose boundaries form the set Λ_0. Pick one of these rectangles inside which $Z(\cdot; L_0)$ has the same sign as μ_2 and denote it by Q. The boundary ∂Q of Q consists of four critical points of Z_0 and four curve segments with finite arclength. Outside each fixed small neighborhood of the critical points, we can solve $Z(L_1, \varphi; L_0) = 0$ by the implicit function theorem for (L_1, φ) as functions of $L_0 \gg 1$ and the arclength parameter s along the curve segments in ∂Q. Furthermore, these functions satisfy

$$
D_{L_0}(L_1, \varphi)(s, L_0) = \mathrm{O}(e^{-\kappa L_0}) \tag{3.21}
$$

uniformly in s. Next, we discuss the set $\Lambda(L_0)$ near each of the four critical points. Pick one of these four and recall that we have shown above that $Z(\cdot; L_0)$ has a unique critical point nearby. Furthermore, this L_0-dependent critical point of $Z(\cdot; L_0)$ of saddle type and nondegenerate. Thus, we can apply the Morse lemma to show that, after a smooth coordinate transformation of (L_1, φ) that depends also smoothly on L_0, the function $Z(\cdot; L_0)$ near the critical point is given by

$$
Z(x, y; L_0) = x^2 - y^2 - \tilde{d}_j(x, y, L_0)e^{-2\alpha_0(x,y)L_0},
$$

where $|\alpha_0| \geq \kappa > 0$, $|\tilde{d}_j| \geq \eta > 0$, and their derivatives with respect to (x, y, L_0) are bounded. Here, $(x, y) = 0$ corresponds to the critical point $(L_1, \varphi) = (L_1^0, \varphi^0) + (\tilde{L}, \tilde{\varphi})$ constructed above. It is now straightforward to solve $Z(x, y; L_0) = 0$ for (x, y) as functions of L_0 and the arclength parameter s, and we again find that the associated functions $(L_1, \varphi)(s, L_0)$ satisfy the estimate (3.21). Thus, using uniqueness of solutions, the different curves we constructed near the curve segments and the critical points fit together to give a

closed curve that lies inside Q and is close to its boundary ∂Q. Furthermore, this solution curve satisfies (3.21).

In summary, we have now solved the Eqs. (3.10)–(3.11), and it remains to solve (3.12) given by

$$v^c(L_1, \varphi, \mu) = \varphi_1(L_0, \mu).$$

Substituting v^c from Lemma 3.2 and φ_1 from (3.5), we obtain the equation

$$L_1 + \varphi + \mathrm{O}(\mathrm{e}^{-\kappa L_1}) = \sigma \left[\phi_j^*(\mu) + \beta_0(\mu) L_0 + a(\phi_j^*(\mu) + \beta_0(\mu) L_0, \mu) + \mathrm{O}(\mathrm{e}^{-\kappa L_0}) \right], \tag{3.22}$$

where $\sigma = \pm 1$, $\mu = z(L_1 - \varphi) + \mathrm{O}(\mathrm{e}^{-\kappa L_1})$, and $(L_1, \varphi) = (L_1, \varphi)(s, L_0)$ are the functions constructed above. Recall that $(L_1, \varphi)(s, L_0)$ stays inside the fixed rectangle Q for all values of (s, L_0). Thus, using (3.21) and the inequality $a_\phi(\phi, \mu) > -1$ that holds for all (ϕ, μ), we can solve (3.22) uniquely for $L_0 = L_0(s)$ for each fixed s. Since $(L_1, \varphi)(s, L_0)$ is a closed curve for each fixed L_0, the resulting solution $(L_0, L_1, \varphi)(s)$ gives closed curve as claimed.

Note that the sign of σ has implications for how L_0 adjusts with (L_1, φ) along each 2-pulse isola. Assume, for instance, that $\sigma = -1$. Upon varying s, the curve $(L_1, \varphi)(s)$ will pass near the boundary of the rectangle Q shown in Fig. 10. Pick the segment along which $\varphi(s)$ is approximately constant, while $L_1(s)$ increases, then (3.22) shows that $L_0(s)$ will actually decrease. Thus, for $\sigma = -1$, if one of L_0 or L_1 increases, then the other variable will decrease, and vice versa. In contrast, if $\sigma = 1$, then both $L_1(s)$ and $L_0(s)$ will increase and decrease together. We remark that we have $\sigma = -1$ near the Turing bifurcations at which the periodic orbits $\gamma(\cdot, \mu)$ emerge from the origin. The computations for the Swift–Hohenberg equation (1.1) that we present in the next section indicate that $\sigma = -1$ for this equation even for parameter values further away from the Turing bifurcation.

4 Discussion

4.1 Summary

Motivated by numerical computations for the Swift–Hohenberg equation, we have analysed the existence of symmetric 2-pulse solutions in homoclinic snaking scenarios. Two-pulse solutions are characterised by two quantities, namely the transition time $2L_0$ near the equilibrium, which measures the separation distance between the two single pulses that form the 2-pulse, and the transition time $2L_1$ near the underlying periodic orbit, which corresponds to the width of the single pulses. We showed that the separation distance and the width of 2-pulses can be parametrized by natural numbers m and n that correspond respectively to the number of oscillations near the equilibrium and to the number of windings that the 2-pulse makes along the periodic orbit. We proved that symmetric 2-pulses exist along a two-parameter family of figure-eight shaped isolas that are parametrized by the integers (m, n). Varying m for fixed n results in a nested family of isolas, while varying n for fixed m gives a stacked family of isolas. Our proof was based on tracking the stable and unstable manifolds of the equilibrium along the underlying heteroclinic cycle whose existence we assumed. To track these manifolds, we used a smooth reversible and symplectic transformation into normal form near the equilibrium and Fenichel coordinates near the periodic orbit. Reversibility then implies that the bifurcation equations for symmetric 2-homoclinic orbits can be viewed as symmetry-breaking perturbations of the

bifurcation equations for symmetric 1-homoclinic orbits: the effect of the symmetry-breaking terms is that the snakes-and-ladder structure of 1-pulses breaks up into figure-eight isolas of 2-pulses. This phenomenon is similar to the effect that forced symmetry-breaking has on the double helix structure of 1-pulses, which was recently explored numerically in [5].

4.2 Connection with Poincare maps

A geometric way of viewing symmetric 2-homoclinic orbits consists of inspecting the dynamics of the Poincare map to a fixed two-dimensional transverse section that is placed at the underlying periodic orbit inside the zero level set of the Hamiltonian. This is illustrated in Fig. 11, where the location of symmetric and non-symmetric 1-homoclinic orbits is shown in the left panel, while the location of symmetric 2-homoclinic orbits is indicated in the right panel. Upon changing the parameter μ, the position of the invariant manifolds will change, and a careful analysis of the geometry in the cross section yields another explanation of homoclinic snaking; see [2,25]. In particular, the fact that $W^s(0, \mu)$ and $W^u(0, \mu)$ are $\mathcal{R}$-images of each other shows that the non-symmetric orbits emerge in pitchfork bifurcations very close to fold bifurcations of symmetric orbits. Symmetric 2-homoclinic orbits can be studied similarly upon making use of the fact that the pull-back $\mathrm{Fix}_0^{\mathrm{pb}}(\mathcal{R})$ of the fixed-point space of the reverser in the transverse section is close to the stable manifold $W^s(0, \mu)$ as indicated in the right panel in Fig. 11. Since the pull-back closely follows $W^s(0, \mu)$, but is not exactly an $\mathcal{R}$-image of $W^u(0, \mu)$, symmetric 2-homoclinic solutions will emerge in fold and not in pitchfork bifurcations, when the curves are moved through each other as the parameter changes.

4.3 Reversibility and Hamiltonian structure

The key structural assumptions on the underlying vector field that we utilised in our analysis are its reversibility and the presence of a Hamiltonian. We now discuss briefly what our expectations are for systems that have only one or none of these structures in place.

First, for generic systems that are neither conservative nor reversible, homoclinic snaking will likely be a codimension-one phenomenon. Indeed, without either of these two structures, we could not assume the generic existence of a heteroclinic cycle that consists of an orbit
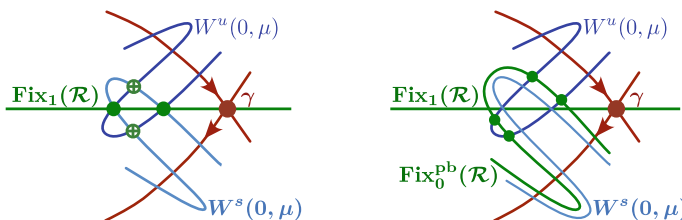

Fig. 11 The *two panels* illustrate the dynamics of the Poincare map associated with a fixed two-dimensional transverse section placed at $\gamma(0, \mu)$ on the periodic orbit. The *left panel* indicates how symmetric (*bullets*) and non-symmetric (*circled crosses*) 1-homoclinic orbits to $u = 0$ arise as intersections of $W^s(0, \mu)$ and $W^u(0, \mu)$: note that symmetric 1-pulses lie in $\mathrm{Fix}_1(\mathcal{R})$. The *right panel* illustrates the location of symmetric 2-homoclinic orbits based on the observation that the pull-back $\mathrm{Fix}_0^{\mathrm{pb}}(\mathcal{R})$ of the fixed-point space of the reverser is close to $W^s(0, \mu)$

that connects $u = 0$ at $x = -\infty$ to the roll pattern at $x = \infty$ and another orbit that connects the roll pattern at $x = -\infty$ with $u = 0$ at $x = \infty$. Codimension-one snaking is discussed further in [7,17] to which we refer for details.

For systems that are Hamiltonian but not reversible, heteroclinic cycles of the type discussed above exist robustly. However, the underlying fronts and backs between $u = 0$ and the roll pattern may appear and disappear independently of each other. We do not know what the resulting homoclinic snaking diagrams would look like but believe that our methods should be applicable to analyse this scenario.

We do not believe that the Hamiltonian structure is essential. It was shown in [2, §6.4] that asymmetric rung states exist even without a Hamiltonian structure; however, these structures will no longer be stationary but will instead move with nonzero speed c of order $\mathrm{e}^{-\eta L_1}$ for some $\eta > 0$ as solutions to the underlying PDE. Combining the ideas in [2, §6.4] with the analysis presented here, it should be possible to show that stationary symmetric 2-pulses exist along figure-of-eight isolas in reversible ODEs without a Hamiltonian structure. Note that symmetric 2-pulses cannot move.

4.4 Hypotheses (H5)–(H6)

We now comment on the role of Hypotheses (H5)–(H6). Snaking was established in [2] under far weaker assumptions on the geometry of the stable and unstable manifolds near the periodic orbit than those encoded in (H5)–(H6). In particular, [2, Hypotheses 6–7] covers the situation where the function $\mu = z(\varphi)$ has several nondegenerate maxima and minima. Furthermore, the modifications outlined in [2, §6.1] allow for isolas of heteroclinic orbits and therefore apply to the case where the stable manifold $W^s(0, \mu)$ is not a graph over the unstable manifold $W^u(\gamma, \mu)$ of the periodic orbit.

We believe that our results for symmetric 2-pulses should be valid also in this more general setting without major complications in the proof. Indeed, our proof relies only on the analysis of the zero level set Λ_0 of the function $Z_0(L_1, \varphi)$ in the (φ, L_1)-plane plotted in Figs. 6 and 10 and then utilises the map

$$(L_1, \varphi) \mapsto (\mu_*(L_1, \varphi), L_1) \tag{4.1}$$

from (3.13) to generate the complete bifurcation diagram. In particular, symmetric 2-pulses exist along the zero level set of the function $Z(L_1, \varphi)$ which is approximately of the form $Z(L_1, \varphi) = Z_0(L_1, \varphi) \pm \eta \mathrm{e}^{-2\alpha_0 L_0}$ for fixed $L_0 \gg 1$ and $\eta > 0$. Hence, the zero level set of Z along which 2-pulses exist can be thought of as the level sets of Z_0 for values slightly higher and lower than zero; see Fig. 10 for an illustration. These arguments should remain valid for more general functions $z(\varphi)$. In Fig. 12, we illustrate the relevant geometry for a function $z(\varphi)$ with four turning points, which occurs in the planar Swift–Hohenberg equation [1]. We expect that symmetric 2-pulses exist along the zero level set of Z which resembles the level sets $Z_0^{-1}(\pm\epsilon)$ of Z_0 for $\epsilon \ll 1$. We refer to Fig. 12iv for an illustration of the anticipated bifurcation diagram of symmetric 2-pulses in the (φ, L_1)-plane.

4.5 Stability

Next, we comment on the anticipated stability properties of symmetric 2-pulses for the Swift–Hohenberg equation. Numerical computations [4] and formal results [2] indicate that the spectrum of 1-pulses is as shown in Fig. 13. The two eigenvalues that move back and forth as each snaking curve of symmetric 1-pulses is traversed cause folds and the pitchfork
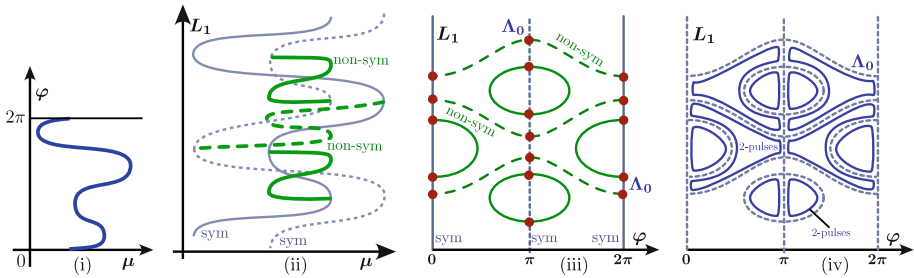
Fig. 12 Panels (**i**) and (**ii**) show a function $\mu = z(\varphi)$ with more than four turning points and the resulting snaking diagram of symmetric and non-symmetric 1-pulses from [2]. Panel (**iii**) illustrates the corresponding zero level set $\Lambda_0 = Z_0^{-1}(0)$ of the function $Z_0(L_1, \varphi)$ whose image under the map (4.1) gives panel (**ii**). We believe that symmetric 2-pulses exist along curves that, roughly speaking, are close to the level sets $Z_0^{-1}(\pm\epsilon)$ of Z_0, where $0 < \epsilon \ll 1$ depends on L_0 as in Sect. 3.3. These are indicated in panel (**iv**)
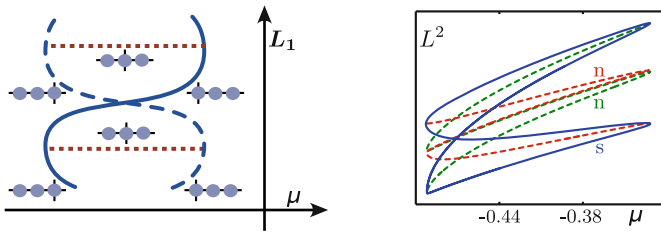

Fig. 13 The *left panel* contains a sketch of the anticipated PDE spectra of symmetric and non-symmetric 1-pulses along part of the double helix. The *right panel* contains the results of numerical computations of the Swift–Hohenberg equation (1.1): shown are an isola of symmetric 2-pulses (labelled (s)) and two z-shaped branches (labelled (n)) of non-symmetric 2-pulses that emerge at pitchfork bifurcations from the symmetric 2-pulse isola

bifurcations to non-symmetric 1-pulses. The results in [22,23] imply that each 1-pulse eigenvalue creates two eigenvalues of the symmetric 2-pulse that we constructed in this paper, provided $m \gg 1$ is sufficiently large; recall that m parametrizes the admissible separation distances L_0 within the 2-pulse. In particular, the translation eigenvalue at zero of the 1-pulse creates the translation eigenvalue of the symmetric 2-pulse and a second eigenvalue that is stable for even indices m and unstable for odd m (or vice versa); see [22,23]. These results together with the form of the isolas of symmetric 2-pulses described here show that symmetric 2-pulses undergo pitchfork bifurcations near each of the folds along the isola on which they lie. The numerical computations presented in Fig. 13 show that the bifurcating non-symmetric 2-pulses lie on z-shaped branches; we believe that they can be predicted using the approach established in [2, Fig. 1.7] for non-symmetric 1-pulses.

4.6 Other multi-pulses

The non-symmetric 2-pulses corresponding to the z-shaped branches shown in Fig. 13 consist of two 1-pulses with roughly the same number of interior rolls. It is conceivable that non-symmetric 2-pulses that consist of two 1-pulses with different numbers of interior rolls exist also. Indeed, Fig. 14 contains such 2-pulses for (1.1), and we refer to [15] for a more comprehensive study of such pulses. All non-symmetric 2-pulses that we computed so far whose underlying 1-pulses have a different number of interior rolls lie on isolas. Using the
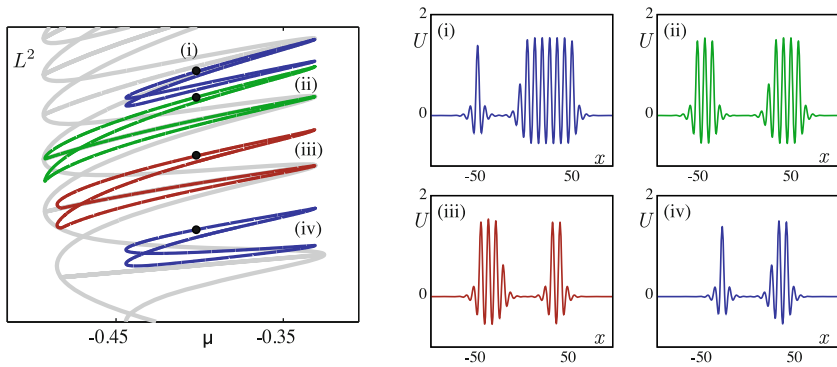
Fig. 14 The *left panel* contains four isolas of non-symmetric 2-homoclinic orbits of (1.1) together with the 1-pulse double-helix structure plotted in *light gray*. Representative profiles of solutions along each of the isolas are plotted in the right four panels
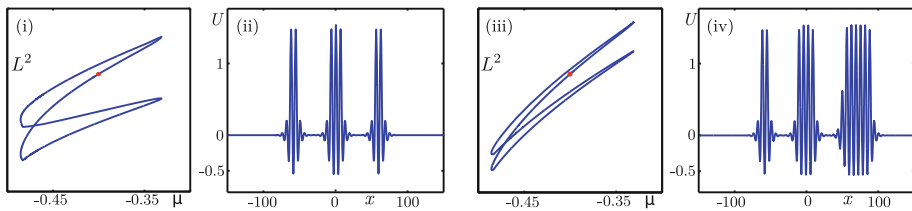

Fig. 15 Panels (**i**) and (**iii**) contain solution branches of, respectively, symmetric and non-symmetric 3-pulses of (1.1). Sample profiles of symmetric and non-symmetric pulses along these branches are shown in panels (**ii**) and (**iv**), respectively

smooth linearization around $u = 0$ and following the approach we employed in Sect. 3, it is not difficult to derive the bifurcation equations that describe non-symmetric 2-pulses with transition times $L_{\pm}$ near the periodic orbit and separation distance L_0 near $u = 0$. Preliminary calculations indicate that non-symmetric 2-pulses comprised of 1-pulses with different numbers of interior rolls always lie on isolas: Without more detailed knowledge about certain higher-order terms, however, it seems difficult to predict the actual shape of the isolas, and we leave this issue for future work. Finally, we expect that N-pulses with $N \geq 3$ behave in a similar fashion. Figure 15 contains computations of symmetric and non-symmetric 3-pulses of (1.1) that lie again on isolas, and we refer to [15] for additional computations.

References

1. Avitabile, D., Lloyd, D.J.B., Burke, J., Knobloch, E., Sandstede, B.: To snake or not to snake in the planar Swift–Hohenberg equation. SIAM J. Appl. Dynam. Syst. **9**, 704–733 (2010)
2. Beck, M., Knobloch, J., Lloyd, D.J.B., Sandstede, B., Wagenknecht, T.: Snakes, ladders, and isolas of localised patterns. SIAM J. Math. Anal. **41**, 936–972 (2009)
3. Belitskii, G.R., Kopanskii, A.Y.: Sternberg theorem for equivariant Hamiltonian vector fields. Nonlinear Anal. **47**, 4491–4499 (2001)

4. Burke, J., Knobloch, E.: Localized states in the generalized Swift–Hohenberg equation. Phys. Rev. E **73**, 056211 (2006)
5. Burke, J., Houghton, S.M., Knobloch, E.: Swift–Hohenberg equation with broken reflection symmetry. Phys. Rev. E **80**, 036202 (2009)
6. Burke, J., Knobloch, E.: Multipulse states in the Swift–Hohenberg equation. In: Hou X., Lu X., Miranville A., Su J., Zhu J. (eds.) Dynamical Systems and Differential Equations, pp. 109-117 (2009)
7. Champneys, A.R., Kirk, V., Knobloch, E., Oldeman, B.E., Rademacher, J.D.M.: Unfolding a tangent equilibrium-to-periodic heteroclinic cycle. SIAM J. Appl. Dyn. Syst. **8**, 1261–1304 (2009)
8. Champneys, A.R., Toland, J.F.: Bifurcation of a plethora of multi-modal homoclinic orbits for autonomous Hamiltonian systems. Nonlinearity **6**, 665–721 (1993)
9. Chapman, S.J., Kozyreff, G.: Exponential asymptotics of localised patterns and snaking bifurcation diagrams. Physica D **238**, 319–354 (2009)
10. Coullet, P., Riera, C., Tresser, C.: Stable static localized structures in one dimension. Phys. Rev. Lett. **84**, 3069–3072 (2000)
11. Dawes, J.H.P.: The emergence of a coherent structure for coherent structures: localized states in nonlinear systems. Phil. Trans. R. Soc. A **368**, 3519–3534 (2010)
12. Devaney, R.L.: Homoclinic orbits in Hamiltonian systems. J. Differ. Equ. **21**, 431–438 (1976)
13. Härterich, J.: Cascades of reversible homoclinic orbits to a saddle-focus equilibrium. Physica D **112**, 187–200 (1998)
14. van der Heijden, G.H.M., Champneys, A.R., Thompson, J.M.T.: Spatially complex localisation in twisted elastic rods constrained to a cylinder. Int. J. Solids Struct. **39**, 1863–1883 (2002)
15. Houghton, S.M., Wagenknecht, T.: Multi-pulses in the Swift–Hohenberg equation with broken symmetry (2010) (in preparation)
16. Knobloch, E.: Spatially localized structures in dissipative systems: open problems. Nonlinearity **21**, T45–T60 (2008)
17. Knobloch, J., Rieß, T., Vielitz, M.: Nonreversible homoclinic snaking (2010) (preprint)
18. Kozyreff, G., Chapman, S.J.: Asymptotics of large bound states of localised structures. Phys. Rev. Lett. **97**, 044502 (2006)
19. Lerman, L.M.: Dynamical phenomena near a saddle-focus homoclinic connection in a Hamiltonian system. J. Stat. Phys. **101**, 357–372 (2000)
20. Moser, J.: On the generalisation of a theorem of A. Liapounoff. Comm. Pure Appl. Math. **11**, 257–271 (1958)
21. Oldeman, B.E., Champneys, A.R., Krauskopf, B.: Homoclinic branch switching: a numerical implementation of Lin's method. Int. J. Bif. Chaos **13**, 2977–3000 (2003)
22. Sandstede, B.: Stability of multiple-pulse solutions. Trans. Am. Math. Soc. **350**, 429–472 (1998)
23. Sandstede, B.: Instability of localized buckling modes in a one-dimensional strut model. Philos. Trans. R. Soc. Lond. A **355**, 2083–2097 (1997)
24. Wadee, M.K., Coman, C.D., Bassom, A.P.: Solitary wave interaction phenomena in a strut buckling model incorporating restabilisation. Physica D **163**, 26–48 (2002)
25. Woods, P.D., Champneys, A.R.: Heteroclinic tangles and homoclinic snaking in the unfolding of a degenerate reversible Hamiltonian Hopf bifurcation. Physica D **129**, 147–170 (1999)